ORIGINAL PAPER

Non-Linear Elasto-Plastic Behaviour of Lacustrine Clay

S. Messerklinger · S. M. Springman

Abstract The paper presents the experimental investigation and analysis of the non-linear elasto-plastic stress–strain behaviour of normally consolidated lacustrine clay. Drained triaxial stress path tests were performed on natural block samples of Swiss lacustrine clay. Data were analysed using plasticity theory and the shape and extent of kinematic yield and bounding surfaces were determined and found to be elliptical but not congruent. Cross-anisotropic elasticity was used to quantify elastic strains to permit plastic strain increment vectors and hence a plastic potential surface to be defined.

Keywords Non-linear · Elasto-plastic ·
Yield surface · Bounding surface · Plastic strain
vector · Lacustrine clay · Anisotropy

1 Introduction

Analyses of soil-structure interaction require the prediction of deformations, both in the surrounding soil mass and within the new construction itself. It has been known for over three decades that ground movements, for example outside excavations in fine-grained soils, cannot be described sufficiently by linear elastic models (e.g. Burland 1989; Burland and Hancock 1977), irrespective of whether the soils are normally consolidated or heavily overconsolidated. Nonetheless, linear elastic perfectly plastic models are still commonly used for calculations of deformations at working load conditions. This has provided the motivation to investigate non-linear elasto-plastic behaviour of deposits of lacustrine clays in Switzerland, which are mainly concentrated in the 'Mittelland', between the Alps and the Jura mountains. This region is also the most densely populated and hence places complex demands on sustainable, lifelong performance of key infrastructure.

The objectives of the presented study are:

(a) to identify the shape and extent of a kinematic yield and the bounding surface
(b) to determine the plastic potential surfaces.

Before presenting the findings, a brief summary is given about:

(a) the characteristics of lacustrine clay,
(b) the test data evaluation method and
(c) the assumptions applied.

2 Lacustrine Clay

Lacustrine clays are deposits that can be found in appropriate geological and geomorphological conditions

S. Messerklinger (✉) · S. M. Springman
Institute for Geotechnical Engineering, ETH Zurich,
Wolfgang-Paulistrasse 15, 8093 Zürich, Switzerland
e-mail: sophie.messerklinger@igt.baug.ethz.ch

S. M. Springman
e-mail: sarah.springman@igt.baug.ethz.ch

Fig. 1 Sample of Swiss lacustrine clay taken in Wauwil from a depth of 27 m, showing the typical varved texture of fine-grained lacustrine deposits (ruler unit in centimetres)

all around the world e.g. Quigley (1983), Diaz-Rodriguez et al. (1992), DeGroot and Lutenegger (2003) and, with particular reference to this study, in the pre-alpine areas of Germany (e.g. Scherzinger 1991), Austria (Schweiger and Breymann 2005) and Switzerland (Heil et al. 1997; Springman et al. 1999). A typical characteristic of lacustrine clays is the distinct stratification (varving[1]) of thin layers of clay and silt (Fig. 1), which results in a structurally anisotropic material (Mitchell 1976).

2.1 Lacustrine Clays in Switzerland

Areas of Switzerland have been covered by glaciers for several periods during the last 1.5 million years, and a detailed picture of the occurrence of ice ages and the extent of the Swiss alpine ice shield is given in Labhart (1995). The last ice age that caused extensive glaciation was the Würm period (Penck 1925). Since then, rivers have transported enormous quantities of sediment and suspended particles into lakes, where they have been deposited as lacustrine deposits at a rate dependent upon the rate of flow through the lakes and their petrology (Van Husen 1987).

---

[1] Varve: "A sedimentary lamina or sequence of laminate deposited in a body of still water within 1 year's time; specif. a pair of layers seasonally deposited in a glacial lake. A glacial varve normally includes a lower "summer" layer consisting of light-colored sand or silt, which grades upwards into a thinner "winter" layer, consisting of clayey, often organic, dark sediment." (Bates and Jackson 1984).

Table 1 Classification of Kloten clay

Plastic limit w_P (%)	14.4
Liquid limit w_L (%)	26.7
USCS classification	CL
Liquidity index I_L (–)	0.98
Grain content < 0.002 mm (%)	21
Activity I_A (–)	0.59
Specific density ρ_s (t/m^3)	2.74

Most of these deposits have consolidated under their own self weight and have not been loaded temporarily by ice or other sediment since then. However, a small degree of overconsolidation results from the increase of the effective stresses due to changes in the water table and from secondary consolidation (Bjerrum 1967; Parry and Wroth 1981). Consequently, these post-glacial deposits tend to be normally consolidated and their fine-grained fraction is called normally consolidated lacustrine clay or "soft Swiss lacustrine clays". Their properties have been described in more detail by Bucher (1975), Gyger et al. (1976), Scherzinger (1991), Amann et al. (1992), Rey (1994), Heil et al. (1997), Springman et al. (1999), Plötze et al. (2003) and Trausch Giudici (2004).

2.2 Kloten Clay

The soft Swiss lacustrine clay investigated in this paper was sampled at a highway construction site in Kloten, an industrial suburb to the north-east of Zurich, close to the international airport. Block sampling techniques were developed in order to minimize disturbance. Samples were extracted as described in Messerklinger (2006) and Messerklinger and Springman (2009). This Kloten clay is classified as low plastic Clay, CL, after USCS (Table 1).

3 Triaxial Test Programme

3.1 The Test Setup and Equipment

Twelve Test specimens were trimmed from the block samples to a diameter of 50 mm and a height of 100 mm and were tested in triaxial stress path test
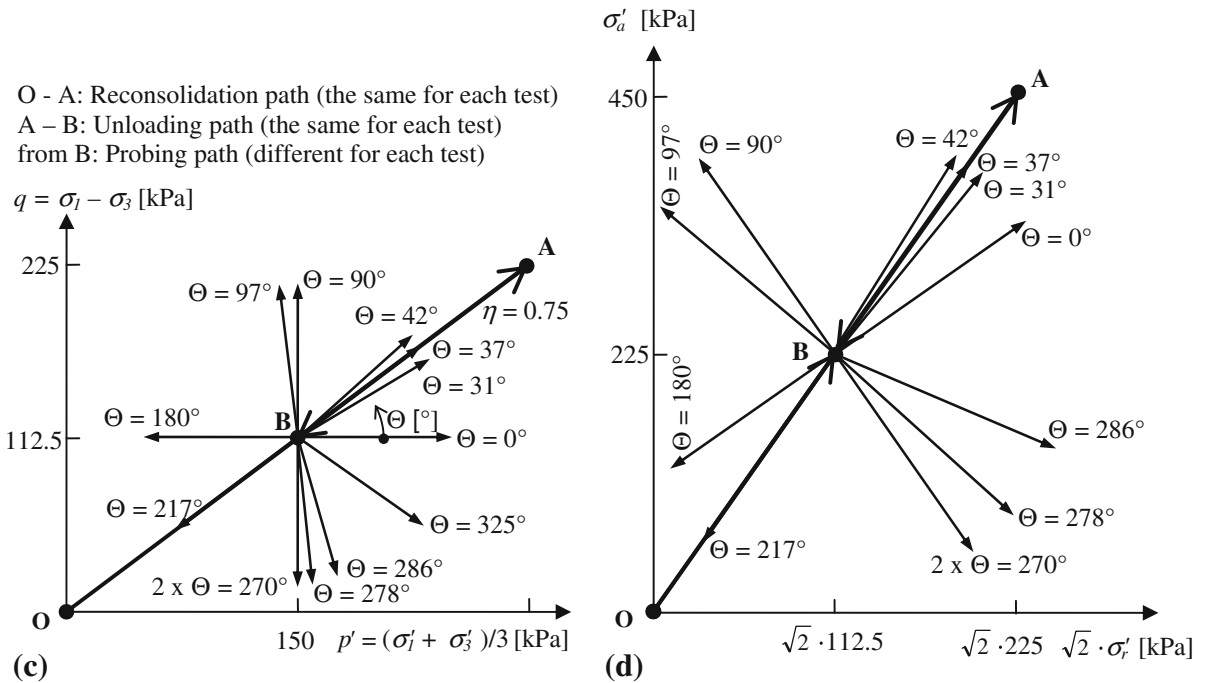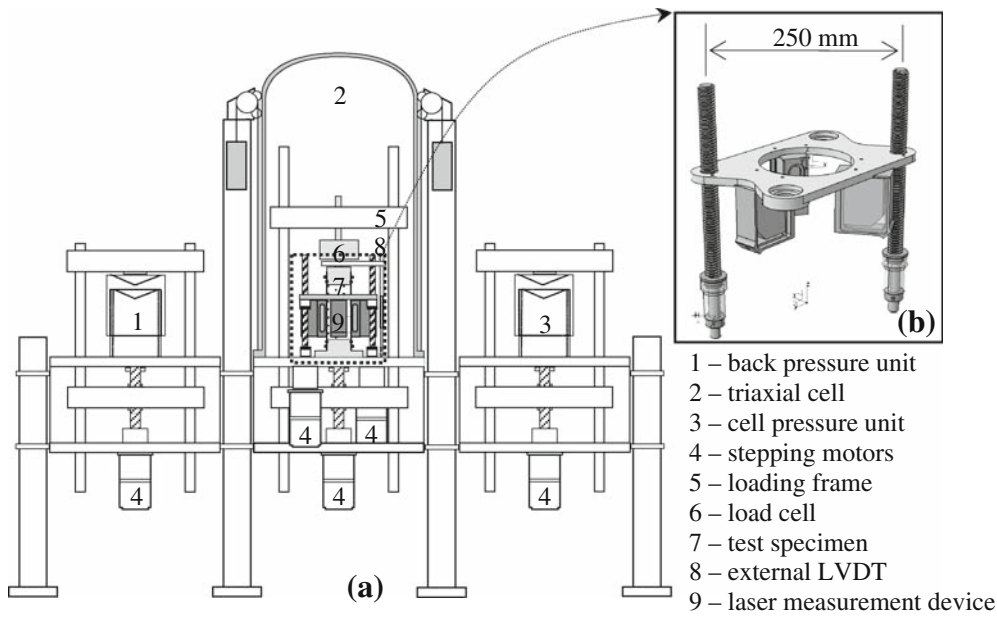
Fig. 2 a Test apparatus; **b** radial displacement measurement device (sketches from Messerklinger and Springman 2007). Consolidation and probing stress paths presented in the **c** $q-p'$ stress space and in the **d** $\sigma'_a - \sqrt{2}\sigma'_r$ stress space

apparatuses, equipped with internal LVDTs for local axial displacement measurement (Messerklinger 2006) and laser transducers for local radial displacement measurement (Messerklinger and Springman 2007; Messerklinger et al. 2004). The triaxial apparatuses (Fig. 2a and b) were built by the

Institute's[2] workshop and allow automated stress path testing in compression and extension (Trausch Giudici 2004).

3.2 The Consolidation Paths

Each specimen was *reconsolidated* along the stress ratio of $\eta = q/p' = 0.75$ with a loading rate of $\Delta p' = 1.0$ kPa/h to a stress state of $q = 225$ kPa and $p' = 300$ kPa. (Fig. 2c: reconsolidation stress path from point O to point A, definition of stress invariants is given in Fig. 2c).

This consolidation path written in effective axial (σ'_a) and radial stresses ($\sqrt{2}\sigma'_r$) gives a stress ratio of $\sqrt{2}\sigma'_r/\sigma'_a = 0.7$ and a corresponding consolidation stress state of $\sigma'_a = 450$kPa and $\sqrt{2}\sigma'_r = \sqrt{2} \cdot 225 = 318.2$kPa (Fig. 2d). This lies far beyond the pre-consolidation stress state of the Kloten clay, which is about $\sigma'_v = 135$ to 180kPa (Messerklinger 2006).

Subsequently, each specimen was *unloaded* along the same stress ratio of $\eta = 0.75$ or $\sqrt{2}\sigma'_r/\sigma'_a = 0.7$, with the same loading rate of $\Delta p' = 1.0$ kPa/h, to a stress state of $q = 112.5$ kPa and $p' = 150$ kPa or $\sigma'_a = 225$kPa and $\sigma'_r = 112.5$kPa, respectively (Fig. 2 c, d: unloading stress path from point A to point B).

These consolidation and unloading paths were applied to all 12 test specimens.

3.3 The Probing Stress Path

Subsequently, the *probing stress path* was applied by loading each specimen under drained conditions, with a loading rate of $|\Delta p'|$ and $|\Delta q'| \leq 1.0$ kPa/h, along a constant stress ratio until failure or far beyond the consolidation stress state.

The different probing stress paths applied to the test specimens are shown in Fig. 2c and d in the $q-p'$ and $\sigma'_a - \sqrt{2}\sigma'_r$ stress space, respectively. The name of the single tests is defined by the angle (Θ) of the stress path in the $q-p'$ space to the horizontal line (Fig. 2c).

4 Data Evaluation and Analysis

4.1 The Background

The triaxial test data obtained from these twelve probing stress paths were analysed using plasticity theory (e.g. Hill 1950), where it is assumed that the total strains are composed of elastic (recoverable) and plastic (irrecoverable) components. The boundary
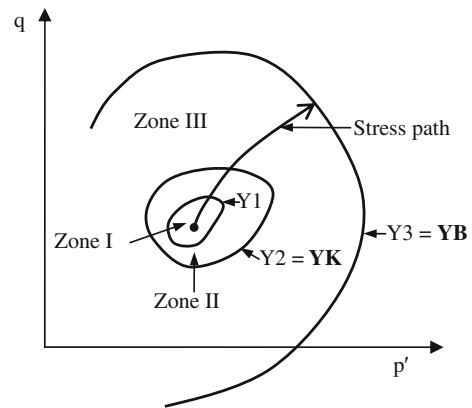
Fig. 3 Identification of Zones I, II and III in triaxial stress space after Jardine (1992). Identification of yield surfaces Y1, Y2 and Y3 in triaxial stress space after Smith et al. (1992). A kinematic yield (YK) and a bounding (YB) surface are defined

between the elastic and the elasto-plastic space is described by the bounding[3] surface.

As long as the current stress path moves inside the bounding surface, elastic strains develop, which are described by the compliance matrix. Stress states outside the bounding surface are not possible. When the stress path reaches the bounding surface, the surface either moves together with the stress path, which is called kinematic hardening (Prager 1955) or it expands, which is called isotropic hardening (Hill 1950). Plastic strains (ε^p) develop with such movements or expansions, which are additional to the elastic strains (ε^e), and these accumulate as total strains ($\varepsilon = \varepsilon^e + \varepsilon^p$), causing a decrease in stiffness.

Nested yield surfaces can be defined inside the bounding surface, to represent several changes in elastic stiffness, which provide an opportunity to model a more realistic non-linear elastic stress–strain behaviour (e.g. Al-Tabbaa and Wood 1989; Mróz 1967; Prévost 1977; Stallebrass and Taylor 1997). Jardine (1992) and Smith et al. (1992) divided the elastic space inside the bounding surface into three zones:

– Zone I: linear elastic zone
– Zone II: recoverable elastic zone
– Zone III: primarily plastic zone

---

[3] Subsequently, the surface between the elastic and the elasto-plastic space will be called bounding surface (YB) and surfaces situated inside the bounding surface will be named yield surfaces.

These three zones were zoned by two kinematic yield surfaces (Y1 and Y2 = YK, Fig. 3). However, the linear elastic Zone I is very small (extending for approximately $\Delta q = \Delta(\sigma_1 - \sigma_3) = 0.5$ kPa and $\Delta\varepsilon_s = 2\Delta(\varepsilon_1 - \varepsilon_3)/3 = 0.001\%$; Smith et al. 1992 or $\Delta q = 1$ kPa and $\Delta\varepsilon_s = 6.10^{-4}\%$ Teachavorasinskun 1989) and can not be determined with the used triaxial test apparatuses. Therefore, the linear elastic zone is not evaluated from the data and is not discussed further in this paper.
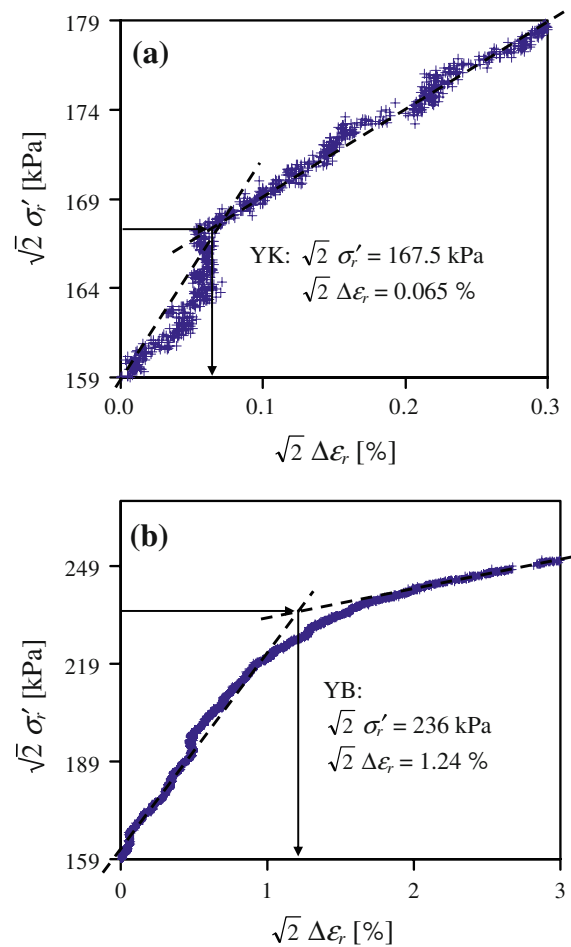
4.2 The Data Evaluation Method

The purpose of the investigations presented in this paper is to evaluate:

– the size and shape of the kinematic (YK) and the bounding surfaces (YB), by identifying changes in stiffness;
– the ratio of the plastic strain increment vectors at the YK and YB surfaces, respectively, and
– the corresponding plastic potential surface by applying a cross-anisotropic elastic model to describe the elastic behaviour.

4.3 Yield Stress States of the Kinematic Yield and Bounding Surface

4.3.1 Data Evaluation

The data evaluation method is highlighted on the stress–strain data of the probing stress path of test $\Theta = 270°$ (Fig. 2), which are plotted at different scales for the determination of the yield and bounding surface (Fig. 4). The origin of stresses in these plots is the post-consolidation stress ($\sigma_a' = 225$kPa, $\sigma_r' = 112.5$kPa and $\sqrt{2}\sigma_r' = 159$kPa, respectively) and the strains are set to zero. Figure 4a presents the stress–strain curve at the start of the probing path for a stress range from $\sqrt{2}\sigma_r' = 159$ to 179kPa and a corresponding radial strain increment range of $\sqrt{2}\Delta\varepsilon_r = 0–0.3\%$. The curve indicates a change in gradient, when fitted with two lines,[4] at a radial effective stress of


Fig. 4 Yield point evaluation method presented on the data of a test with $\Theta = 270°$ **a** $\sqrt{2}\sigma_r' - \sqrt{2}\Delta\varepsilon_r$ plot for $\sigma_a' - \sqrt{2}\sigma_r'$, determination of a possible yield state at a kinematic surface YK; **b** $\sqrt{2}\sigma_r' - \sqrt{2}\Delta\varepsilon_r$ plot for $159 \leq \sqrt{2}\sigma_r' \leq 269$kPa, determination of a yield state at a bounding surface YB

$\sqrt{2}\sigma_r' = 167.5$kPa, with a corresponding radial strain increment of $\sqrt{2}\Delta\varepsilon_r = 0.065\%$. This is the first detectable kink in the stress–strain curve and is selected to represent the stress state on the yield surface (YK). This point is added to Fig. 5 (red open square) where the data are presented in the $\sigma_a' - \sqrt{2}\sigma_r'$ and $\varepsilon_a - \sqrt{2}\varepsilon_r$ space, respectively, to analyse the plastic potential surface from the plastic strain increment

---

[4] Methods for defining the yield stress (e.g. Casagrande, 1936; Tavenas et al., 1979) were reviewed by Messerklinger (2001) for use in numerical simulations with elasto-plastic constitutive models. Methods that could be implemented were summarized and it was concluded that the intersection of two straight lines

Footnote 4 continued
approximating the test results was the best method for evaluating the yield stress, when the data are used for elasto-plastic models. Therefore, a simple bi-linear approach was applied for the data evaluation, which was also used by Koskinen et al. (2002) and Özbas et al. (2004).
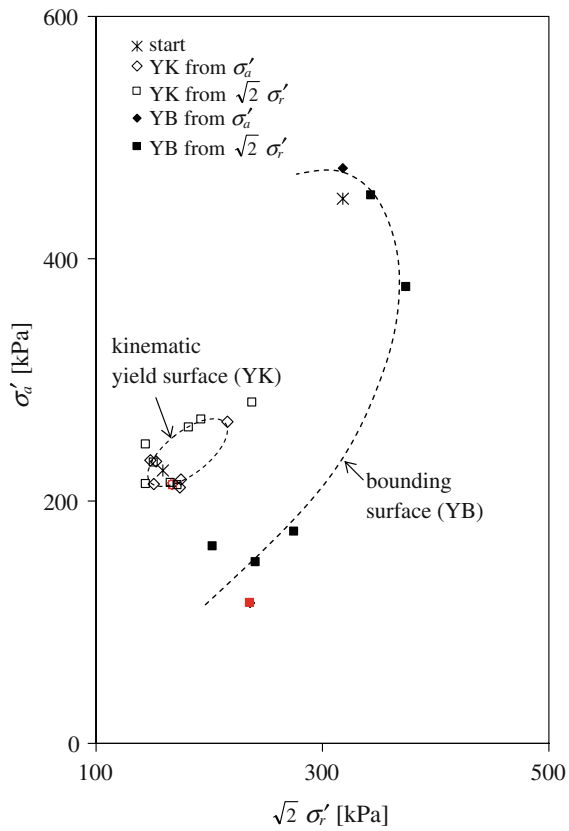
Fig. 5 Summary of yield stress states of a kinematic yield and a bounding surface. The *open squares* represent the first yield stress state detected from the radial effective stress versus radial strain plot. The *open rhombuses* represent the first yield stress state detected from the axial effective versus axial strain plot. These first yield stress states are interpreted as the kinematic yield surface (YK). The *closed squares* represent the second yield stress state detected from the radial effective stress versus radial strain plot. The *closed rhombuses* represent the second yield stress states detected from the axial effective versus axial strain plot. These second yield stress states are at the bounding yield surface (YB). This plot is presented in the more common stress invariant $q-p'$ stress space in Messerklinger (2006)

vectors assuming the energy function to be $\delta W = \delta\sigma'_a\delta\varepsilon_a^p + 2\delta\sigma'_r\delta\varepsilon_r^p$ (e.g. after Schofield and Wroth 1968; or Gudehus 1979).

Figure 4b presents the stress–strain curve over a larger range. The plot shows the transition from the elastic to the elasto-plastic state at around $\sqrt{2}\sigma'_r = 236$kPa (with a corresponding radial strain increment of $\sqrt{2}\Delta\varepsilon_r = 1.24\%$), which was selected to represent the stress state at the bounding surface (YB) This point is as well added to Fig. 5 (red square). The same evaluation was done with the test data plotted in the $\sigma'_a - \Delta\varepsilon_a$-space.

Data from all of the twelve triaxial stress path tests were evaluated in this way, with further details available in Messerklinger (2006). Yield points at YK and YB were not visible in every stress–strain curve and for all tests, so further analysis was restricted only to those stress points for which a significant change in gradient was detected. These were added to Fig. 5 and used for further comparative studies.

The yield stress points were summarized in a $\sigma'_a - \sqrt{2}\sigma'_r$ plot (Fig. 5), with those derived from the $\sigma'_a - \Delta\varepsilon_a$ plot named "from σ'_a" and those obtained from the $\sqrt{2}\sigma'_r - \sqrt{2}\Delta\varepsilon_r$ plot described "from $\sqrt{2}\sigma'_r$". The crosses in Fig. 5 indicate the starting point of the probing stress path (at $\sigma'_a = 225$kPa and $\sigma'_r = 112.5$kPa), and the pre-consolidation stress state (at $\sigma'_a = 450$kPa and $\sigma'_r = 225$kPa).

The results obtained for the yield stress states delineating the kinematic surface (YK) and the bounding surface (YB) determined from the $\sigma'_a - \Delta\varepsilon_a$ plot and the $\sqrt{2}\sigma'_r - \sqrt{2}\Delta\varepsilon_r$ plot are quite consistent. The only two points that are slightly inconsistent are the yield points of the boundary surface for the two stress path tests in extension ($\theta = 270°$, Fig. 3), where one point lies within the implied surface and two are located beyond it. The yield stress state at the bounding surface is already close to, or at, the failure stress state, whereby the varving strongly influences the response at failure with abrupt shearing along a horizontal silt layer in the necking zone (Messerklinger 2006). Therefore, the failure stress state of the extension tests was observed to be highly dependent on the number and thickness of the silt layers located in the necking zone. Consequently, some variation in stress states representing a predicted bounding surface was expected for stress path tests in extension, with yield stress states close to failure.

4.3.2 Data Analysis

Yield stress points defining a kinematic surface (YK) can be fitted by a curve with an elliptical shape, with an extension of $\Delta\sigma'_a = 56$ and $\sqrt{2}\Delta\sigma'_r = 70$kPa, inclined at about 37° to the $\sqrt{2}\sigma'_r$ axis (Fig. 5). Another curve was fitted through yield stress points representing a bounding surface (YB). The shape of this curve (Fig. 5) forms almost a quarter of an ellipse, which is not quite congruent with the ellipse indicated by the yield points of the kinematic yield surface (YK).

Neither surface passes through the crosses describing the initial extreme stress state following stress reversal since each surface extends in the direction of the preceding stress path. This might be explained by creep, accompanying some fabric destructuration, as noticed e.g. by Clayton and Heymann (2001), who allowed rest periods of up to 12 days between consolidation and subsequent stress paths for accurate measurement of very small strains following stress reversal. The rest period between the consolidation, swelling and subsequent shearing in the tests presented in this paper was only 24 h, whereas the loading rate applied during the stress path of $\left|\Delta\sigma'_a\right|$ & $\left|\Delta\sigma'_r\right| \leq 1.5$ kPa/h, designed to represent drained conditions, led to a test duration of more than

Consequently, the elastic stress–strain behaviour needs to be determined to be able to calculate the plastic strain vector from the total strain vector. The stiffness decreases with increasing strain since the stress–strain behaviour is non-linear and highly dependent on the strain magnitude applied. The elastic stiffness at the "very small"[5] strain range is of interest here.

4.4.2 Elastic Strain Component

A cross-anisotropic elastic model e.g. after Barden (1963), defined by five independent material parameters as given in the compliance matrix in Eq. 1 for the triaxial stress space, was applied:

$$
\begin{bmatrix}
\Delta\varepsilon_a \\
\Delta\varepsilon_r \\
\Delta\varepsilon_r \\
\Delta\gamma_{ar} \\
\Delta\gamma_{ra} \\
\Delta\gamma_{rr}
\end{bmatrix}
=
\begin{bmatrix}
1/E_a & -v'_{ar}/E_a & -v'_{ar}/E_a & & & \\
-v'_{ar}/E_a & 1/E_r & -v'_{rr}/E_r & & & \\
-v'_{ar}/E_a & -v'_{rr}/E_r & 1/E_r & & & \\
& & & 1/G_{ar} & & \\
& & & & 1/G_{ar} & \\
& & & & & 2(1+v'_{rr})/E_r
\end{bmatrix}
\begin{bmatrix}
\Delta\sigma'_a \\
\Delta\sigma'_r \\
\Delta\sigma'_r \\
\Delta\tau_{ar} \\
\Delta\tau_{ra} \\
\Delta\tau_{rr}
\end{bmatrix}
\tag{1}
$$

35 days. Although the low plasticity Kloten clay (Table 1) is not particularly susceptible to creep, some time effects may have occurred during this comparably long test period, which were not investigated at this stage.

4.4 Plastic Potential at the Kinematic Yield and Bounding Surface

4.4.1 Data Evaluation

The shape of the plastic potential surface is identified from the *plastic* strain vector at the yield stress state, which can be derived from the *total* strain vector (sum of plastic and elastic components) measured during the triaxial tests. Some authors assume that the elastic component of strains is small enough during plastic straining, compared to the plastic component, to be ignored. This might be acceptable for straining beyond the bounding surface, but it can not be applied for straining between the kinematic and the bounding surface.

---

[5] In general, elastic strains for which elastic parameters are more or less independent of axial strain (c.$<10^{-3}\%$) are defined as being "very small" (Atkinson and Sällfors 1991) compared to "small" strains of the order of $10^{-2}\%$. The accuracy of the axial strain measurement system falls between both values at $4 \times 10^{-3}\%$ (Messerklinger 2006).

Despite progress in measurement of very small strains in triaxial devices (Jardine et al. 1984; Clayton and Khatrush 1986; Hird and Yung 1989; Goto et al. 1991), Atkinson and Sällfors (1991) among others contend that even special triaxial apparatuses and local strain measurement devices are not able to measure the "very small" strain stiffness. The "very small" elastic shear modulus can be measured, for example, by using a piezoceramic bender element to generate shear waves at one end of a specimen, and determine their travel time through the soil to the other end of the specimen by a second bender element (e.g. Dyvik and Madshus 1985; Viggiani and Atkinson 1995 or Mohsin and Airey 2003). Although some authors maintain that the elastic stiffness determined from bender element tests is lower than the theoretical elastic stiffness (Jardine 1992), which is due to slipping and fretting at particle contacts even at very small strains, as pointed out by Bowden and Tabor (1964) and Johnson (1985), this remains difficult to quantify. The assumption made in this paper is that the shear modulus determined from bender element measurements represents the "very small strain" elastic stiffness.

where E_a is the stiffness in the axial, E_r is the stiffness in radial direction, v'_{ar} is the Poisson's ratio between the axial and radial directions, v'_{rr} is the Poisson's ratio between two radial directions and G_{ar} is the shear modulus.

Three parameters (v'_{ar} and b^6) were determined from the stress strain curves at the start of the probing stress path to be (for more details see Messerklinger (2006)):

$$v'_{ar} = 0.52 \quad E_a = 120 \text{ MPa} \quad b = 8.7\,10^{-6}\,[1/\text{kPa}].$$

.

These values represent the stiffness at "small" strains corresponding to the accuracy of the displacement measurement devices in the triaxial test apparatus.

Bender element tests, which apply shear strains of less than $10^{-3}\%$ (Dyvik and Madshus 1985), were performed at the consolidation stress state of $\sigma'_a = 225$kPa and $\sigma'_r = 112.5$kPa and the shear modulus at the "very small" strain range was determined to be $G_{ar} = 98$ MPa.

Unfortunately, the shear modulus can not be determined directly from triaxial test data. Therefore, the *modified* cross-anisotropic stiffness matrix after Graham and Houlsby (1983) was used, which introduces an anisotropy factor α relating the two Young's moduli ($E_r/E_a = \alpha^2$) and the two Poisson's ratios ($v'_{rr}/v'_{ar} = \alpha$) to each other. The shear modulus was then calculated from $v'_{ar} = 0.52$; $E_a = 120$ MPa and $b = 8.7\,10^{-6}$ [1/kPa]) to be $G_{ar} = 32.7$ MPa.

The elastic shear modulus derived from the triaxial test data in the "small" strain range ($G_{ar,\text{Triax}} = 32.7$ MPa) is a factor of 3 smaller compared to the "very small" strain shear modulus obtained from the bender element tests ($G_{ar,\text{Bender}} = 98$ MPa). This factor was applied to upscale the stiffness parameters derived from the triaxial test data.

– The axial stiffness (E_a,) was up-scaled by the factor of 3 to $E_a = 360$ MPa.
– Both Poisson's ratios (v'_{rr} and v'_{ar}) were kept the same as anisotropy is expected to change

primarily with plastic straining and the plastic strain component at a shear strain magnitude of $10^{-3}\%$ is zero or so small that this still remains a reasonable assumption.
– The parameter b was downscaled by the factor of 3 to $b = 2.9\,10^{-6}$ [1/kPa] E_r by the same amount, while v'_{rr} stays constant.

Consequently, the cross-anisotropic elastic parameters adopted for the determination $v'_{ar} = 0.52$ of the plastic strain vector are: $E_a = 360$ MPa, and $b = 2.9\,10^{-6}$ [1/kPa].

Having applied the modified cross-anisotropic stiffness matrix after Graham and Houlsby (1983) already for the shear modulus, it can also be used to calculate the ratio between the axial and radial Young's moduli to be $E_a/E_r = 1.73$. Finally, the value of the parameter b determined from the cross-anisotropic elastic model is compared to the corresponding value from an isotropic elastic model, by matching up the stiffness matrices against each other. The results are summarized in Fig. 6 and show that all materials with a b value larger than the corresponding isotropic elastic value $b = (1 - v')/E$ are stiffer axially than radially, which is the case here, assuming the modified cross-anisotropic stiffness matrix after Graham and Houlsby (1983) to be valid.
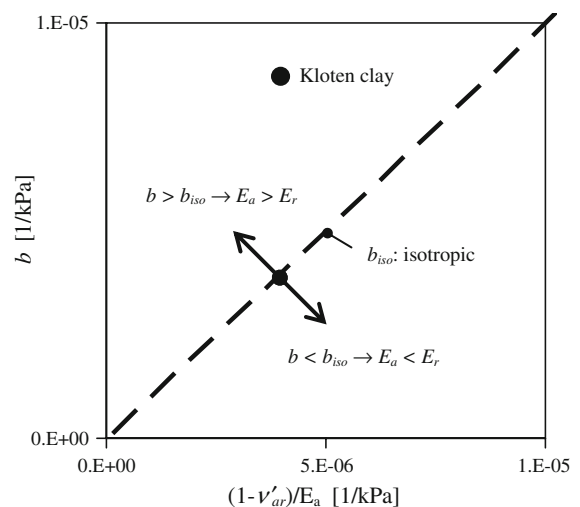
Fig. 6 Comparison of the cross-anisotropic value of the parameter b to the corresponding isotropic value b_{iso}

---

[6] If cell pressure is applied to a specimen under triaxial loading conditions, the parameters v'_{rr}, E_r and G_{ar} can not be determined explicitly from the resulting triaxial test data. Therefore, v'_{rr} and E_r are summarised as a composite parameter $b = (1 - v'_{rr})/E_r$

4.4.3 Plastic Strain Increment Vector

Finally, the plastic strain vectors at the corresponding yield stress states (YK & YB respectively, Fig. 8) can be determined from the total strain vectors by applying the cross-anisotropic elastic compliance matrix in the "very small" strain range derived above. An incremental response envelope, as originally introduced by Gudehus (1979), was used to present the size of the plastic strain increment vector. Results are examined for a unit stress increment of a fixed magnitude ($\sqrt{\left(\Delta\sigma_a'^2 + 2\Delta\sigma_r'^2\right)} = 10\text{kPa}$) applied at the yield points, but varying in direction (corresponding to the stress path).

The method adopted to evaluate data and to determine the plastic strain increment vector at the kinematic yield point is highlighted below, using the test data of the probing stress path of test $\Theta = 270°$ (Fig. 2). Figure 7a presents the stress–strain curve at the start of the probing stress path. The curve indicates a change in gradient at $\sqrt{2}\sigma_r' = 167.5\text{kPa}$, which represents the stress state at the kinematic yield surface (YK, see Chap. 4.3.1). The unit stress increment of 10 kPa is applied starting at the yield point and following along the probing stress path of

test $\Theta = 270°$, which is $\Delta\sigma_a'/\Delta\sigma_r' = minus; 2$. Consequently, the component of the unit stress increment along the σ_r' axis is calculated to be $\sqrt{2}\Delta\sigma_r' = \sqrt{\left\{\left(200 / \left[\left(\left(\Delta\sigma_a'/\Delta\sigma_r'\right)^2 + 2\right)\right]\right)\right\}} = 5.77\text{kPa}$ and the corresponding radial plastic strain increment is determined from the test data to be $\Delta\ \sqrt{2}\Delta\varepsilon_r^p = 0.11\%$ (Fig. 7a).

In the axial versus radial plastic strain plot (Fig. 7b), the corresponding plastic axial strain increment was determined as $\Delta\ \Delta\varepsilon_a^p = -0.017\ [\%]$. Therefore, the plastic strain increment vector $\Delta\ \Delta\varepsilon_a^p / \Delta\sqrt{2}\Delta\varepsilon_r^p$ (for a unit stress vector of 10 kPa) is known and can be added to the yield point (red line, Fig. 8a).

This procedure was repeated for all YK and YB points. Results from all of the twelve stress path tests are summarised in Fig. 8.

The plastic strain increment vector (Fig. 8b) would be drawn perpendicular to a tangent to the plastic potential surface, which would indicate that the shape of such a plastic potential surface must be similar to that of the presumed boundary surface that has been drawn with a dashed line. The same analysis is done for the YK yield points (Fig. 8a). The plastic strain vectors at the YK have significant variations in the
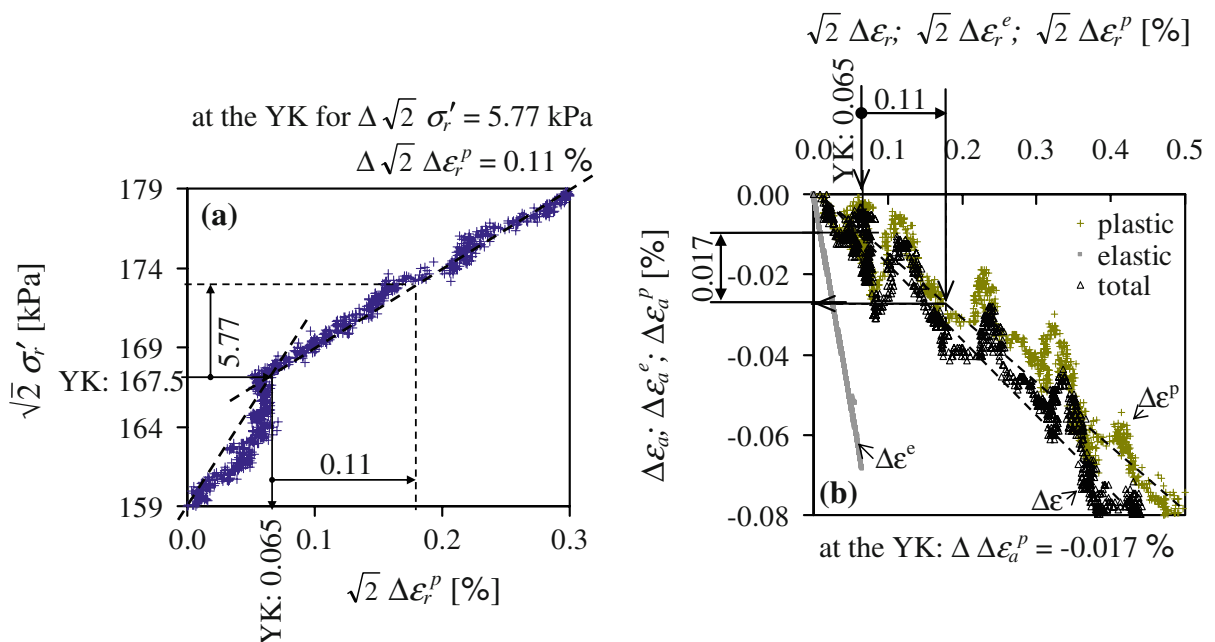
Fig. 7 Determination of the plastic strain increment vector on the kinematic yield surface (YK) presented for the test data with $\Theta = 270°$: **a** determination of $\Delta\ \sqrt{2}\ \Delta\varepsilon_r^p$ at the YK for a unit stress increment of 10 kPa; **b** determination of $\Delta\ \Delta\varepsilon_a^p$ at the YK for the strain increment $\Delta\ \sqrt{2}\ \Delta\varepsilon_r^p = 0.11\%$ (determined in Fig. 7a)
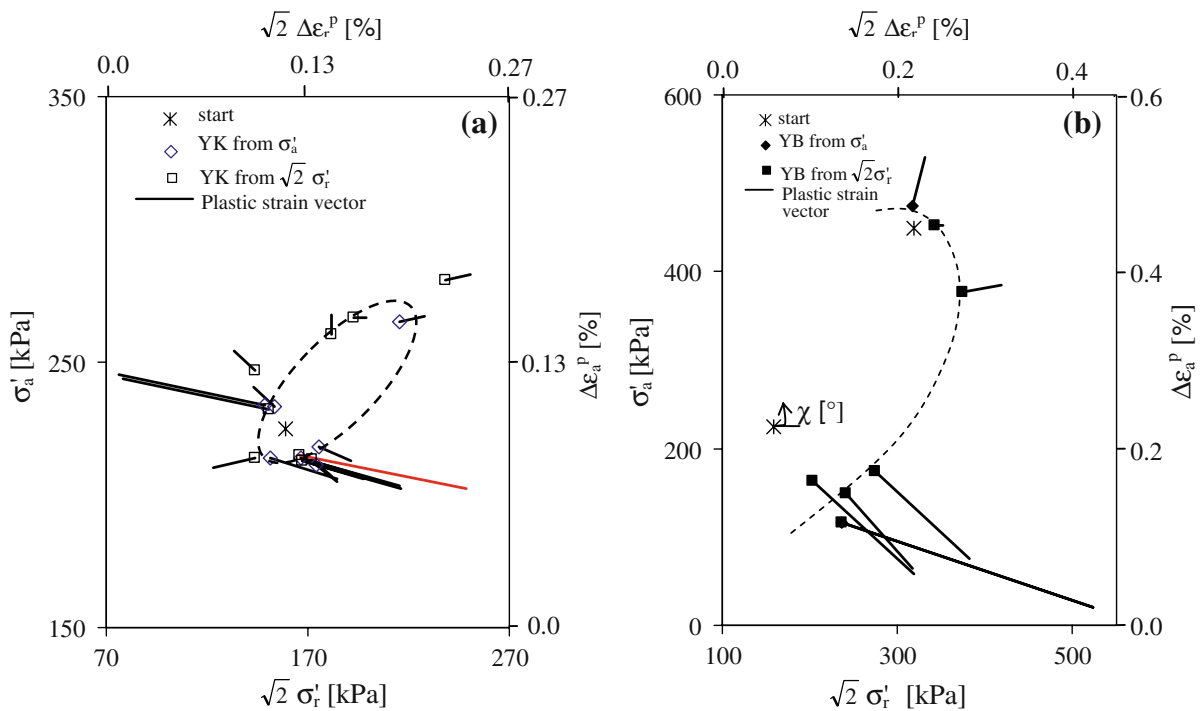
Fig. 8 Plastic strain vector, for a unit stress increment of ($\sqrt{(\sigma_a'^2 + 2\sigma_r'^2)} = 10$ [kPa], at the corresponding yield stress states of **a** the kinematic yield surface (N.B.: non-zero origin) and **b** the bounding surface, presented in the $\sigma_a'(\Delta\varepsilon_a) - \sqrt{2}\sigma_r'(\sqrt{2}\Delta\varepsilon_r)$ stress (plastic strain increment) space

Table 2 Comparison for the flow rule

Sector/yield surface	YK	YB
$0 < \chi < 90°$	Partly associated	Mainly associated
$90 < \chi < 180°$	Partly associated	No values obtained
$180 < \chi < 270°$	Partly associated	No values obtained
$270 < \chi < 0°$	Mainly non-associated ($+\Delta\varepsilon_r^p$ is relatively larger than $-\Delta\varepsilon_a^p$ in most cases)	Mainly associated

direction and only about half of them would imply associated flow.

A comparison of the tangents to the plastic potential surface to the shape of the proposed yield surface is shown in Table 2.

5 Conclusion

This analysis of the twelve drained triaxial stress path tests on natural lacustrine clay investigated the deformation response of varved soils. Yield points, and the direction of the total strain increment ratio at these yield points, were determined from the relevant stress–strain plots. The shape of the kinematic yield surface and the bounding surface was established. It was found that the bounding surface has an elliptical shape within boundaries constrained by failure in compression and extension, which is not congruent with the elliptical shape of the kinematic surface, but inclined from the radial effective stress axis towards the positive axial effective stress axis.

The total strains at yield were split into the elastic and the plastic components for the identification of the shape of the plastic potential from the plastic strain increment ratios, by applying a cross-

anisotropic elastic compliance matrix. Three stiffness parameters were calculated from the triaxial strain measurement data for "small" strains from which the shear modulus was estimated by applying the simplified cross-anisotropic elastic compliance matrix (Graham and Houlsby 1983). This shear modulus was compared to the value obtained from measurements with bender elements, which gave a scaling factor for the elastic parameters of 3, based on the assumption that the anisotropy is unaffected by shearing up to "very small" strains.

Consequently, the shape of the plastic potential was determined. The comparison between the plastic potential surface derived, and the proposed yield surfaces, showed that an associated flow rule is appropriate for the kinematic and bounding surfaces in those quadrants of the $\sigma'_a - \sqrt{2}\sigma'_r$ stress space that were removed from failure occurring in compression or extension.

References

Al-Tabbaa A, Wood DM (1989) An experimental based "bubble" model for clay. In: Pietruszczak S, Pande GN (eds) Proceedings of the 3rd international symposium on numerical models in geomechanics, Canada, pp 91–99

Amann P, Bucher F, Heil HM (1992) Untersuchungen an Seebodenlehm. Mitteilungen des Institutes für Geotechnik No. 4391, ETH Zürich

Atkinson JH, Sällfors G (1991) Experimental determination of stress-strain-time characteristics in laboratory and in situ tests. In: Proceedings of the 10th ECSMFE, Florence, vol 3, pp 915–956

Barden L (1963) Stresses and displacements in a cross-anisotropic soil. Géotechnique 13(3):198–210

Bates RL, Jackson JA (1984) Dictionary of geological terms. 3rd edn prepared by the American Geological Institute. Doubleday Dell Publishing Group, Inc.: 551

Bjerrum L (1967) Engineering geology of Norwegian normally-consolidated marine clays as related to settlements of buildings. 7th Rankine lecture. Géotechnique 17(2):83–119

Bowden FP, Tabor D (1964) The friction and lubrication of solids. Oxford University Press, London

Bucher F. (1975). Die Restscherfestigkeit natürlicher Böden, ihre Einflussgrössen und Beziehungen als Ergebnis experimenteller Untersuchungen." PhD thesis, Nr.: 5523. Mitteilungsheft Nr.: 103, Institut für Geotechnik, ETH Zürich

Burland JB (1989) Small is beautiful - the stiffness of soils at small strains. 9th Laurits Bjerrum memorial lecture. Can Geotech J 26:499–516

Burland JB, Hancock RJR (1977) Underground car park at the house of commons, London: geotechnical aspects. Struct Eng 55:87–100

Casagrande A (1936) The determination of the pre-consolidation load and its practical significance. In: Discussion D-34, Proceedings of the 1st ICSMFE, vol 3. Cambridge, pp 60–64

Clayton CRI, Heymann G (2001) Stiffness of geomaterials at very small strains. Géotechnique 51(3):245–255

Clayton CRI, Khatrush SA (1986) A new device for measuring local axial strains on specimens. Géotechnique 36(4):593–597

DeGroot DJ, Lutenegger AJ (2003) Geology and engineering properties of connecticut valley varved clay. In: Tan TS, Phoon KK, Hight DW, Leroueil S (eds) Proceedings of the characterisation and engineering properties of natural soils, vol 1. Singapore, Balkema, Rotterdam, pp 693–724

Diaz-Rodriguez JA, Leroueil S, Aleman JD (1992) Yielding of Mexico city clay and other natural clays. J Geotech Eng 118(7):981–995

Dyvik R, Madshus C (1985) Laboratory measurements of G_{max} using bender elements. Advances in the art of testing soils under cyclic conditions. ASCE, New York, pp 186–196

Goto S, Tatsuoka F, Shibuya S, Kim Y-S, Sato T (1991) A simple gauge for local small strain measurements in the laboratory. Soils Found 31(1):169–180

Graham J, Houlsby GT (1983) Anisotropic elasticity of a natural clay. Géotechnique 33(2):165–180

Gudehus G (1979) A comparison of some constitutive laws for soils under radially symmetric loading and unloading. In: Wittke W (ed) Proceedings of the 3rd international conference numerical methods in geomechanics. Aachen, vol 4. pp 1309–1323

Gyger M, Müller-von Moos M, Schindler K (1976) Untersuchungen zur Klassifikation spät- und nacheiszeitlicher Sedimente aus dem Zürichsee. Schweizerische mineralogische und petrographische Mitteilungen, Heft 56: 387–406

Heil HM, Huder J, Amann P (1997) Determination of shear strength of lacustrine clays. In: Proceedings of the 14th ICSMFE, Hamburg, Balkema, Rotterdam. vol 1, pp 507–510

Hill R (1950) The mathematical theory of plasticity. Oxford University Press, London

Hird CC, Yung PCY (1989) The use of proximity transducers for local strain measurements in triaxial tests. Geotech Test J 12(4):292–296

Jardine RJ (1992) On the kinematic nature of soil stiffness. Soils Found 32(2):111–124

Jardine RJ, Symes MJ, Burland JB (1984) The measurement of soil stiffness in the triaxial apparatus. Géotechnique 34(3):323–340

Johnson KL (1985) Contact mechanics. Cambridge University Press, Cambridge

Koskinen M, Karstunen M, Wheeler SJ (2002) Modelling destructuration and anisotropy of a natural soft clay. In: Proceedings of the 5th Europ conference numerical methods in geotechnical engineering, Paris pp 11–20

Labhart TP (1995) Geologie der Schweiz, 3rd edn. Ott-Verlag, Thun

Messerklinger S (2001) Numerical modelling of anisotropy of soft clays. Diploma thesis, Institute for soil mechanics and foundation engineering, Graz University of Technology

Messerklinger S, Bleiker E, Zweidler A, Springman SM (2004) Displacement measurement with laser scanning in triaxial testing apparatuses. In: Proceedings of the 16th Europ young geotechnical engineers conference, Vienna, ISBN 3-902450-51-7, pp 251–260

Messerklinger S (2006) Non-linearity and small strain behaviour in lacustrine clay. Dissertation, No. 16512, ETH Zurich (available online at: http://e-collection.ethbib.ethz.ch)

Messerklinger S, Springman SM (2007) Local radial displacement measurements using laser transducers. Geotech Test J, 30(6):454–465

Messerklinger S, Springman SM (2009) Economic sampling and extraction of undisturbed, high quality samples in normally consolidated lacustrine clays using a large diameter tube. Geotech Geol Eng J 27(2):207–215

Mitchell JK (1976) Fundamentals of soil behaviour. Wiley, New York

Mohsin AKM, Airey DW (2003) Automating G_{max} measurement in triaxial tests. In: Di Benedetto H, Doanh T, Geoffroy H, Sauzéat C (eds) Proceedings of the 3rd international symposium deformation characteristics of geomaterials (ISLYON), Lyon, pp 73–80

Mröz Z (1967) On the description of anisotropic work hardening. J Mech Phys Solids, London 15:163–175

Özbas F, Senol A, Hatipoglu M (2004) The evaluation of pre-consolidation pressure results of "CH" subgrades in terms of various determination methods. In: Proceedings of the 16th Europ young geotechnical engineers' conference, Vienna, ISBN 3-902450-51-7, pp 297–302

Parry RHG, Wroth CP (1981) Shear stress-strain properties of soft clays. Soft clay engineering. In: Brand EW, Brenner RP (eds) Elsevier Scientific Publishing Company, Amsterdam, pp 311–362

Penck A (1925) Glazialgeologische Beobachtungen in den bayerischen Hochalpen: Alte Breccien u. junge Krustenbewegungen in d. bayerischen Hochalpen; Die Eiszeit in den bayerischen Hochalpen." Sitzungsberichte d. Preuss. Akad. d. Wiss. Physik.-math. Klasse 17. Akademie d. Wissenschaften; Berlin. Verlag: W. de Gruyter & Co

Plötze M, Giudici Trausch J, Messerklinger S, Springman SM (2003) Swiss Lacustrine clay: mineralogical and mechanical characteristics. Eds: P.A. Vermeer, H.F. Schweiger, M. Karstunen and M. Cudny. international workshop on geotechnics of soft soils - theory and practice, Noordwijkerhout, The Netherlands, Verlag Glückauf, Essen, pp 473–478

Prager W (1955) The theory of plasticity: a survey of recent achievement. Proc Inst Mech Engs, London 169:41–57

Prévost JH (1977) Mathematical modeling of monotonic and cyclic undrained clay behaviour. Int J Numer Anal Methods Geomechanics 1:195–216

Quigley RM (1983) Glacial Geology—an introduction for engineers and earth scientists. In: Eyles N (ed) Glaciolacustrine and glaciomarine clay deposition: a North American perspective. Pergamon Press, New York, pp 140–167

Rey R (1994) Geotechnische Folgen der glazialen Vorbelastung von Seebodenablagerungen. PhD thesis Nr. 10631, ETH-Zurich, Switzerland

Scherzinger T (1991) Materialverhalten von Seetonen - Ergebnisse von Laboruntersuchungen und ihre Bedeutung für das Bauen im weichen Baugrund." Veröffentlichungen des Inst. für Boden- und Felsmechanik, Karlsruhe, Heft: 122

Schofield AN, Wroth CP (1968) Critical state soil mechanics. McGraw Hill, London

Schweiger H, Breymann H (2005) FE-analysis of five deep excavations in lacustrine clay and comparison with in situ measurements. In: Proceedings of the 5th international symposium geotechnical aspects of underground construction in soft ground, Amsterdam, pp 887–892

Smith PR, Jardine RJ, Hight DW (1992) The yield of Bothkennar clay. Géotechnique 42(2):257–274

Springman SM, Giudici Trausch J, Heil HM, Heim R (1999) Strength of a soft swiss lacustrine clay: cone penetration and triaxial test data. J Transp Res Board 1675:1–9

Stallebrass SE, Taylor RN (1997) The development and evaluation of a constitutive model for the prediction of ground movements in overconsolidated clay. Géotechnique 47(2):235–253

Tavenas F, Des Rosiers JP, Leroueil S, La Rochelle P, Roy M (1979) The use of strain energy as a yield and creep criterion for lightly overconsolidated clays. Géotechnique 29(3):285–303

Teachavorasinskun S (1989) Stress-strain and strength characteristics of granular materials in simple shear. MEng. Thesis, University of Tokyo, Japan

Trausch Giudici J (2004) Stress-strain characteristics of Seebodenlehm. Dissertation, No. 15528, ETH Zürich. (available online at: http://e-collection.ethbib.ethz.ch.)

Van Husen D (1987) Die Ostalpen in den Eiszeiten. Populärwissenschaftliche Veröffentlichungen der geologischen Bundesanstalt, Wien

Viggiani G, Atkinson JH (1995) Interpretation of bender element tests. Géotechnique 45(1):149–154